DEPARTMENT OF
AEROSPACE ENGINEERING

FMLAB

# Investigation of separated flow physics over low-Reynolds-number airfoil via surface and wake measurements

Roi Baruch
Advisor: Dr. Igal Gluzman

June 8, 2025

## Abstract

The flow behavior over an airfoil at low Reynolds numbers (at typical chord Reynolds numbers up to 500,000) is considered to be more complicated than at high Reynolds numbers. At low Reynolds numbers, the initial laminar boundary layer may detach from the airfoil surface, leading to an unstable laminar separation bubble that may lead to a non-abrupt transition to turbulence. Understanding the complex physics of the low Reynolds number flow over an airfoil from surface measurements is vital for flow control applications that aim to increase aerodynamic performance, such as reducing drag due to flow separation. In this study, our objective was to associate the separation flow physics over low-Reynolds-number airfoil (NACA 63-412) to surface pressure data. We conducted wind tunnel experiments—at various angles of attack, up to 14 degrees at Reynolds numbers between 170,000 – 700,000—measuring the surface pressure distribution around the airfoil and at its wake to estimate the drag force. In addition, detailed surface oil flow visualizations are employed to provide qualitative information on the surface flow topology. In particular, relations have been established between the first and second spatial derivatives of the streamwise static surface pressure profile and the detachment and reattachment locations of the separation bubble.

# Contents

**1 Introduction 3**

**2 Experimental Setup 4**
2.1 Wind Tunnel . . . . . . . . . . . . . . . . . . . . . . . . . . . . . . . . 4
2.2 Model Design and Installation . . . . . . . . . . . . . . . . . . . . . . . 5
2.3 Flow Diagnostic Techniques . . . . . . . . . . . . . . . . . . . . . . . . 7
2.3.1 Surface Pressure Measurements . . . . . . . . . . . . . . . . . . 7
2.3.2 Wake pressure . . . . . . . . . . . . . . . . . . . . . . . . . . . . 7
2.3.3 Oil flow visualization . . . . . . . . . . . . . . . . . . . . . . . . 7

**3 XFOIL Analysis 9**
3.1 Setting $N_{crit}$ . . . . . . . . . . . . . . . . . . . . . . . . . . . . . . . 9

**4 Results 10**
4.1 Pressure distribution . . . . . . . . . . . . . . . . . . . . . . . . . . . 10
4.1.1 pressure distribution analysis: WT experiments vs. XFOIL . . . . . . . . . . 10
4.1.2 Transition point identification from pressure profile data . . . . . . . . . . . 12
4.1.3 Separation bubble identification from pressure profile data . . . . . . . . . . 13
4.1.4 Separation detection after transition to turbulence . . . . . . . . . . . . . . . 15
4.2 Oil visualization . . . . . . . . . . . . . . . . . . . . . . . . . . . . . . 17
4.3 Drag calculation from wake measurements . . . . . . . . . . . . . . . . 18

**5 Conclusion 20**

**6 Acknowledgments 22**

**7 Appendix 22**
7.1 Separation line detection . . . . . . . . . . . . . . . . . . . . . . . . . 22

# 1 Introduction

The flow behavior over an airfoil at low Reynolds numbers (at typical chord Reynolds numbers up to 500,000) is common in UAVs and turbomachine blades (Carreño Ruiz et al. 2023; Karasu et al. 2013). At the initial laminar boundary layer may detach from the airfoil surface, leading to an unstable laminar separation bubble (LSB), which can also trigger non-abrupt transition to turbulence (Tank et al. 2017; Schlichting and Gersten 1999). This process is illustrated in Fig. 1. The presence of LSB is considered the main cause for poor performance at low Reynolds numbers and increases the drag.

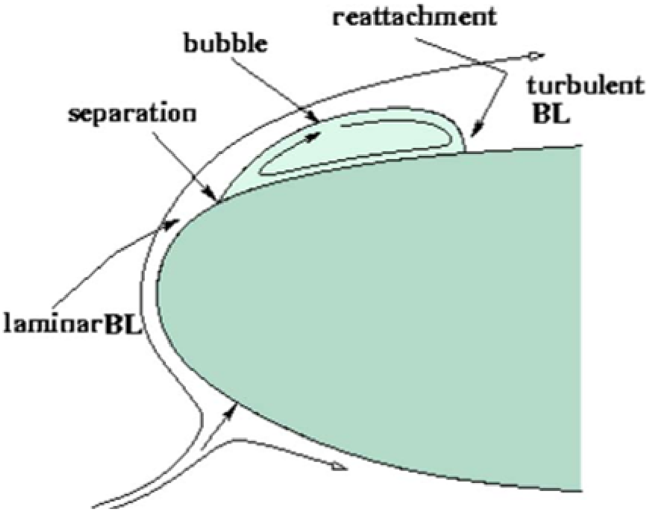

Figure 1: Schematic of a laminar separation bubble formed on a low-Reynolds-number airfoil. Reproduced from Hu and Yang (2008).

Many studies have been devoted to understanding the physical mechanisms that govern LSB, where in particular, recent studies have focused on double separation phenomena, such as the study of Eljack (2024), where the authors investigated the possibility of two separation bubbles forming upon a NACA 0012 airfoil, a leading edge (LE) bubble and a trailing edge (TE) one, and their merging at high angles of attack due to a low-frequency mode. Other studies examined the unstable physics of LSB via both experiments and simulations. For example, the authors in Toppings and Yarusevych (2024) captured the separation bubble using particle image velocimetry (PIV) over a NACA 0018, focusing on the bursting of the bubble and the spanwise structures. In Klose et al. (2025), the authors considered the flow field around a NACA 65(1)–412 airfoil using a DNS simulation, observing the unstable LSB in the time-averaged solution.

In practical cases, it is desirable to gain insights on separation flow physics from a limited and simple set of measurements, such as the pressure profile over an airfoil to improve an airfoil's performance during flight. Early studies, such as Russell (1979), showed that a separation bubble can be identified from its footprint on the pressure surface measurements as seen in Fig. 2. After the suction peak, the pressure coefficient increases, and the flow encounters an adverse pressure gradient. The resulting LSB can be identified via a distinct pressure profile signature on the upper surface of the airfoil, where the pressure coefficient plateaus along the separation bubble region. Further downstream, the pressure coefficient curve drops and merges with the inviscid pressure distribution (distribution that would be obtained without a laminar separation bubble) at the bubble reattachment point. Recently, in Simmons et al. (2024), it was shown that the

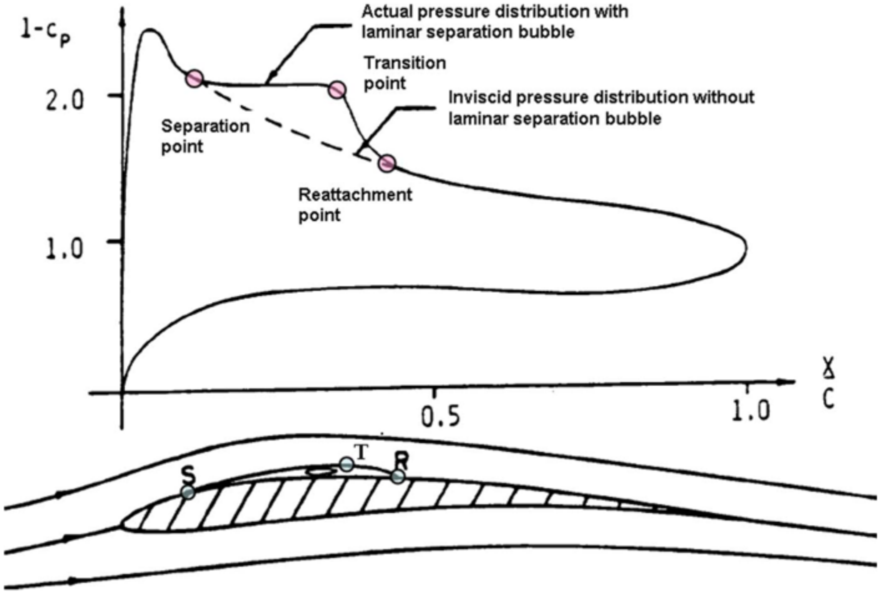

Figure 2: Pressure distribution on an airfoil with laminar separation bubble (Russell 1979).

first and second spatial derivatives of the streamwise static surface pressure profile are sufficient to determine key locations of detachment and reattachment in smooth body turbulent separation flow.

In this study, we extend the application of the in Simmons et al. (2024) to detect the separation and transition locations of the separation bubble in low Reynolds airfoil flow—a more complex case that may include a combination of laminar flow, laminar separation bubble, transition to turbulence, and turbulent separation. Herein we conducted an experimental study over a NACA 63-412 airfoil a range of free-stream velocities from 10 to 40 m/s that would correspond to a range of Reynolds numbers based on the airfoil's cord length of $1.7 \times 10^5 \leq Re \leq 7 \times 10^5$. The streamwise variation of $C_p(x)$,$C_p'(x)$, and $C_p''(x)$ to detect the separation and transition locations of the separation bubble is tested. Our study included measurements of the flow over the airfoil, including surface flow visualization, mean surface pressure measurements, and pressure profiles downstream of the airfoil wake. In addition, due to the sensitivity of the derivatives $C_p'(x)$ and $C_p''(x)$ to the spatial resolution of the obtained pressure profile, a panel code analysis (XFOIL) was used to obtain high-resolution profiles after validating their agreement with experimental data.

The rest of this work is organized in the following order: experimental setup and diagnostic techniques are presented in section 2. Details on XFOIL simulations are provided in section 3. Results are presented in section 4. Finally, conclusions and areas of future development are discussed in section 5.

# 2 Experimental Setup

## 2.1 Wind Tunnel

The experiments were conducted in the Technion's Mach 0.23 (80 m/s) open-return subsonic wind tunnel at the Aerospace Faculty. A side view schematic of the tunnel is shown in Figure 3. The flow is driven by a 400 kW motor that can operate in ranges up to 645 RPM. The inlet has an area ratio of 1:25. Additionally, to lower the turbulence levels of the freestream, eight screens were placed upstream of the inlet, achieving low free-stream turbulence levels below 0.5% for a freestream velocity of 50 m/s. The length of the test section is $3\,m$ with a $1 \times 1\,m$ square cross-section.

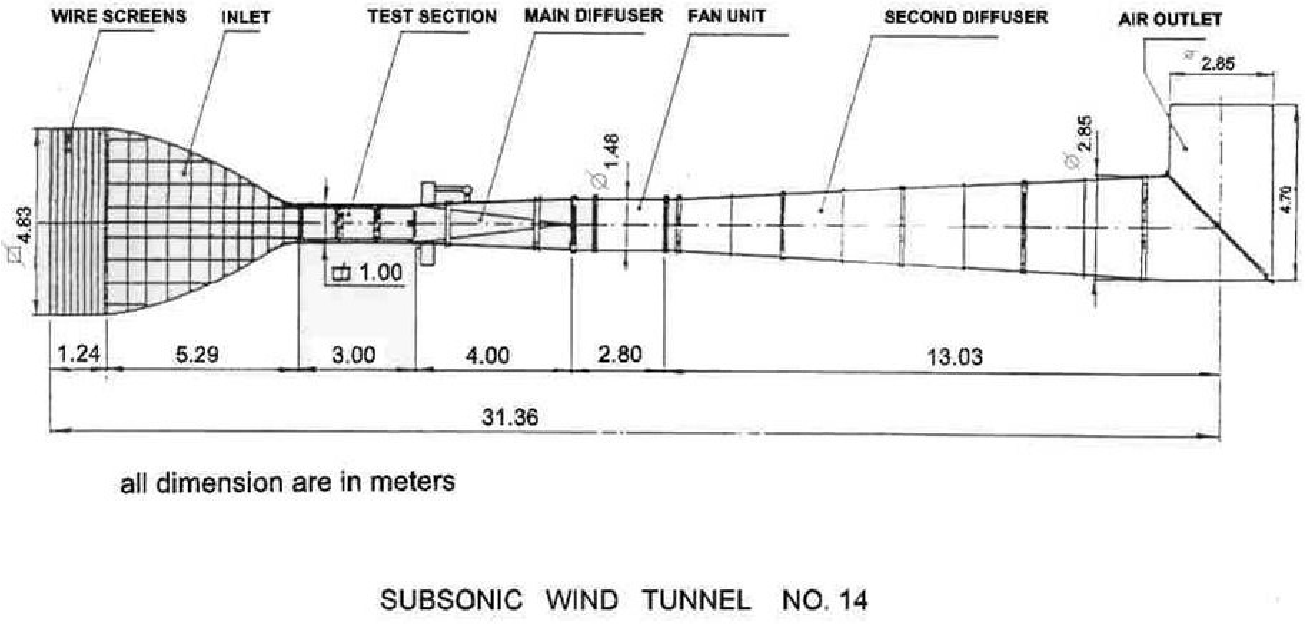

Figure 3: Schematic of the subsonic open-return wind tunnel facility (denoted as Tunnel No. 14) in Technion's Wind Tunnel Complex of the Department of Aerospace Engineering at Technion.

## 2.2 Model Design and Installation

The model geometry was NACA 63-412, this low Reynolds airfoil is illustrated in Fig. 4. The total span of the wing model is 1 meter, spanning across the entire test section as shown in Fig. 5a. The model along the z-axis is assembled from three sections: the middle section, where the pressure taps are located, was fixed to the tunnel between two sections on each side to minimize any 3D effects from the tunnel side walls. The Wing model was connected to the tunnel side walls at two locations, at the top using an aluminum bracket that was free to rotate around itself. The base of the model was connected to a rotating plate at the floor of the wind tunnel (WT) experiments that controlled the angle of attack.

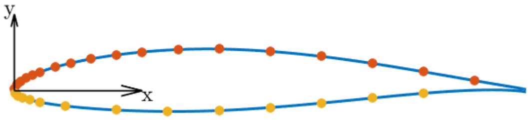

Figure 4: NACA 63-412 geometry, with pressure tap locations markings.

(a) (b)

Figure 5: Experimental setup inside the test section (flow goes from left to right). a) Mounted airfoil model suspended inside the Mach 0.23 wind tunnel test section with pressure rake sensor downstream. b) Enlarged image of the pressure rake sensor downstream of the airfoil geometry.

## 2.3 Flow Diagnostic Techniques

### 2.3.1 Surface Pressure Measurements

The Model is fitted with 32 pressure taps distributed along the top and bottom surfaces at the middle part, as shown in Fig. 4. The location of the pressure taps along the surface is distributed more densely near the leading edge to capture the drastic pressure gradient. Each pressure tap is connected to a pressure gauge using Tygon tubing. The pressure gauges that were used were Honeywell model LM with the following specifications:

- Accuracy - 0.5% full scale.
- Pressure range: 1–2.5 PSIG, depending on the pressure gauge.
- Sample frequency 3 kHz, internally averaged in using block averaging to 10 Hz.

### 2.3.2 Wake pressure

We measured the airfoil drag by obtaining the pressure distribution at the airfoil's wake. In Figs. 5a and 5b, we can see the experiment setup for measuring pressure at the wake.

The pressure measurement device in Fig. 5b includes 21 pressure gauges, 20 total pressure, and the middle pressure gauge measuring the static pressure. From those measurements, The Drag coefficient can be obtained using (Barlow et al. 1999):

$$C_D = 2\int (\sqrt{\frac{H-p}{H_0-p_0}} - \frac{H-p}{H_0-p_0})\frac{dy}{c}, \tag{1}$$

where:

- $H$ - total pressure at the wake.
- $H_0$ - total pressure at the freestream.
- $p$ - static pressure at the wake.
- $p_0$ - static pressure at the freestream.

### 2.3.3 Oil flow visualization

In the second part of the experiment, oil droplets were sprayed on the wing surface to help visualize the streamlines. A combination of oleic acid, titanium dioxide powder, and SAE 60 grade vacuum pump oil was used with a ratio of 1:5:10, respectively, similar to the recipe used in Natarajan et al. (2021). After mixing the ingredients and getting a smooth mixture, small droplets were sprayed over the surface using a small toothbrush. By stroking the toothbrush bristles at a certain distance from the surface at different regions over the surface, a uniform layer of small droplets could be applied evenly over the surface. After spraying the oil, the wind tunnel test section was quickly closed, and the experiments run continuously for approximately 5 minutes. Afterward, the test section was opened, and the model was illuminated with a fluorescent light source, and images were taken using a Canon 5D Mark IV camera. An example of the obtained oil flow pattern is illustrated in Fig. 6.

Figure 6: Example of streamlines from oil visualization obtained at freestream U= 40 m/s.

To highlight the oil pattern, we used MATLAB Image Processing Toolbox, where the following steps are applied:

1. Convert the image to grayscale.
2. Contrast adjustment.
3. Image smoothing via 3 × 3 median filtering to reduce artifacts and noise due to the light source reflections.
4. Sharpening the image, enhancing edge contrast by subtracting the median-filtered image (from the previous step) from the original.
5. Locating the LE and TE of the airfoil geometry in the image by applying a Canny edge detector. Can be seen in Fig. 16 with each 10% of the chord marked in the yellow lines.

An example of a sample image—before and after the above processing procedure—is illustrated in Fig. 7.

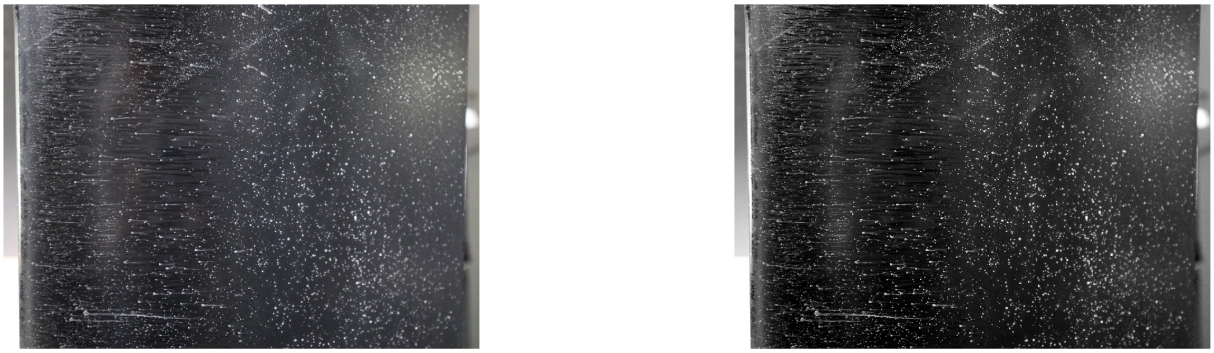

(a) (b)

Figure 7: Example of image processing process for experiment at U = 40 m/s. a) Raw image. b) Processed image.

# 3 XFOIL Analysis

A panel code analysis was conducted to supplement our experimental results and further investigate the separation bubble phenomenon. XFOIL Drela (1989b) is a panel code method written by Mark Drela at MIT that solves both the boundary layer integral equations and potential flow equations. To determine the transition location for the boundary layer, XFOIL uses the $e^N$ amplification formulation. The $N_{crit}$ value is set as default to $N_{crit} = 9$, with the option to manually adjust it as later discussed in section 3.1. The analysis results in the pressure coefficient distribution along the surface, lift and drag value, and the boundary layer parameters, including the transition location. Example of XFOIL performance compared to experimental results is shown in Fig. 8, which is reproduced from Morgado et al. (2016).

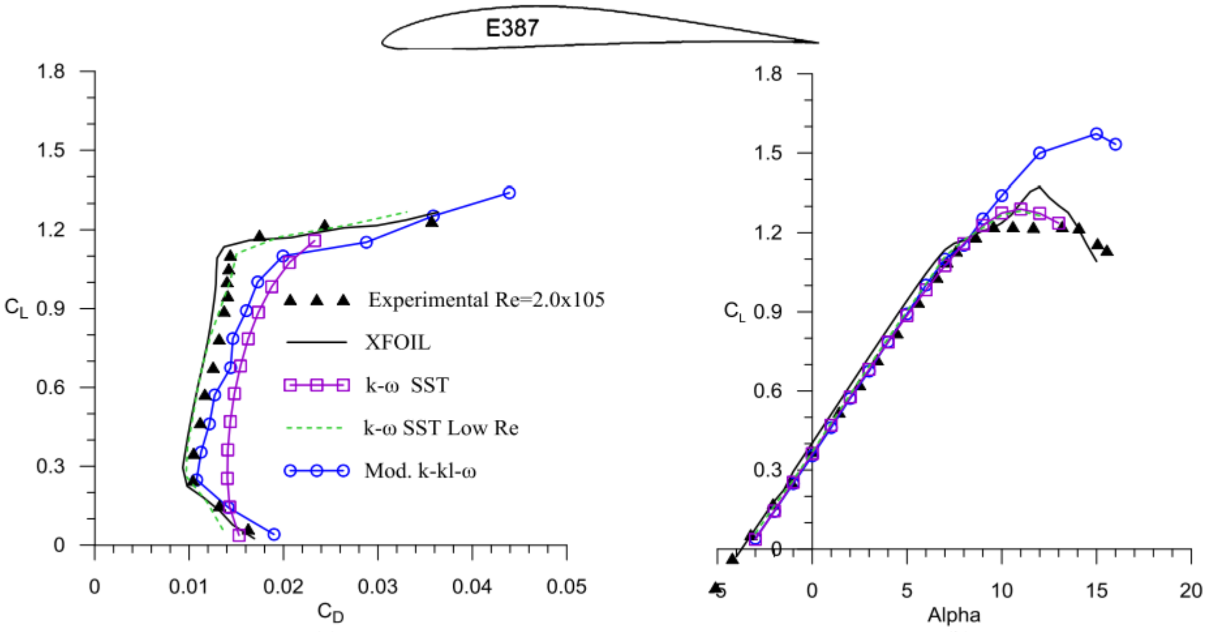

(a) (b)

Figure 8: Aerodynamic characteristics of the E387 airfoil measured at Penn State wind tunnel compared with the numerical simulation results obtained using XFOIL. Plot reproduced from Morgado et al. (2016).

## 3.1 Setting $N_{crit}$

XFOIL predicts the transition point with the $e^N$ method while selecting $N_{crit} = 9$ as a default. We can adjust the $N_{crit}$ value to match the WT experiments experimental results. This value changes with the turbulence level of the WT experiments as described in Drela (1989a), for which the following an empirical relation is proposed:

$$N = -8.34 - 2.4 \cdot ln(\frac{2.7 \cdot tanh(\frac{Tu}{2.7})}{100}), \tag{2}$$

where Tu is the percentage of turbulence levels. In our study, which was conducted in wind-tunnel 14, the turbulence level is assumed to be $Tu = 0.14\%$, which yields $N_{crit} = 7$ using the formula in Eq. (2). We note that the $Tu = 0.14\%$ was based on information available to us regarding the tunnel. To confirm this number, detailed freestream measurements are required, which were not possible in the current experimental campaign. We note that choosing $N_{crit}$ in the range 7-9 had a negligible effect on the results in this study.

# 4 Results

## 4.1 Pressure distribution

### 4.1.1 pressure distribution analysis: WT experiments vs. XFOIL

Herein, we analyze the pressure coefficient distribution over the airfoil, defined as

$$C_p = \frac{p - p_0}{\frac{1}{2}\rho U^2}, \tag{3}$$

where $p_0$ and $U$ are the mean pressure and mean freestream velocity at the inlet of the test-section, and $p$ is the local static pressure over an airfoil.

In Fig. 9, we compare pressure coefficient distribution around the airfoil obtained from pressure taps in WT experiments vs. panel code analysis in XFOIL solver, with the default value for $N_{crit} = 7$.

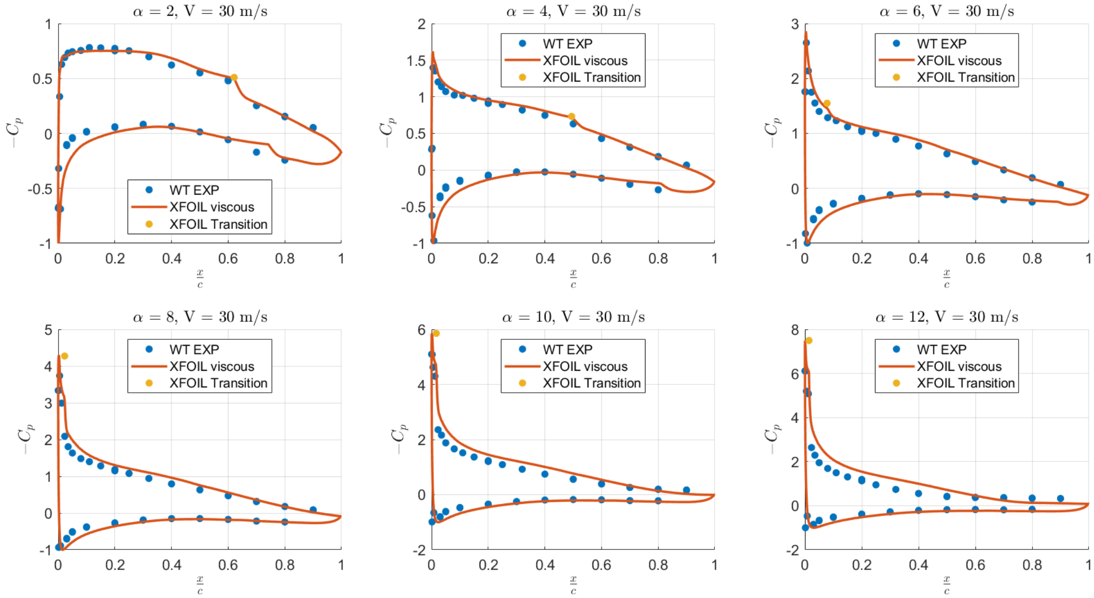

(a) $U = 30$ m/s.

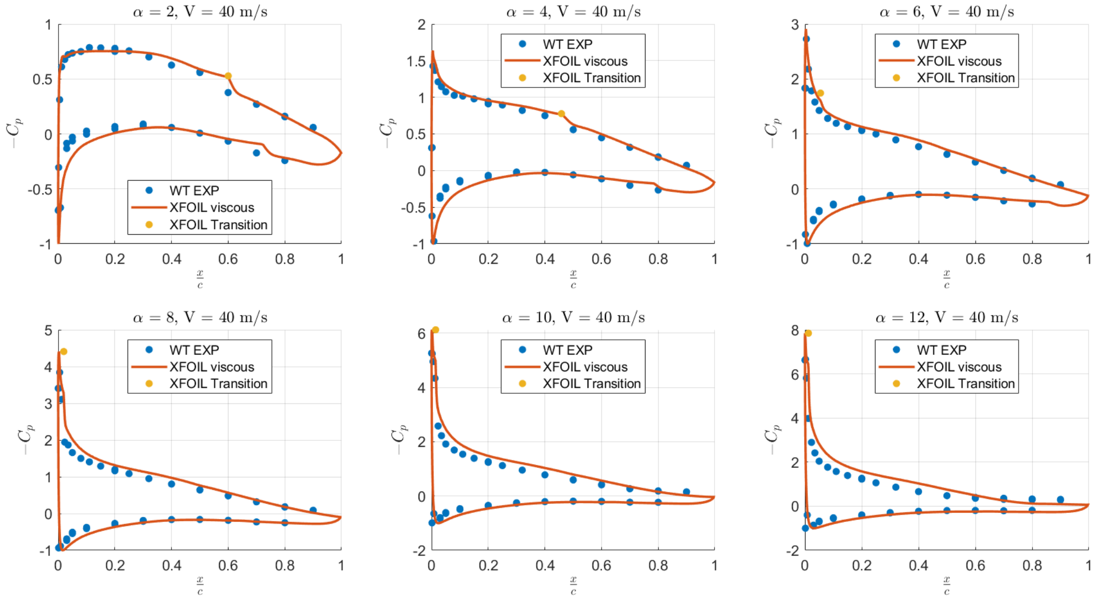

(b) $U = 40$ m/s.

Figure 9: Pressure distribution along both upper and lower surfaces, a comparison between WT experiments vs XFOIL. In a) for 30 m/s b) 40 m/s for $N_{crit} = 7$.

In particular, we compare results for freestream velocities 30, 40 m/s, respectively, and for angles of attack up to $\alpha = 12°$. One can see that we have a good agreement between XFOIL and WT experiments measurements. As the angle of attack increases, we can observe the XFOIL solution starting to deviate from the pressure distribution obtained by WT experiments.

### 4.1.2 Transition point identification from pressure profile data

Herein, we check the relation between the transition point to the pressure gradient as described in section 1. In Fig. 10, we plot the pressure coefficient and its first derivative from both WT experiments and XFOIL over the upper surface, zooming into the first 30% of the chord. In particular, we set $N_{crit} = 7$ determined using Eq. (2). Note that the pressure derivative is plotted with a minus sign and a scaling parameter $S = 0.05$, allowing us to rescale the derivative profile to be visually comparable with pressure profile data.

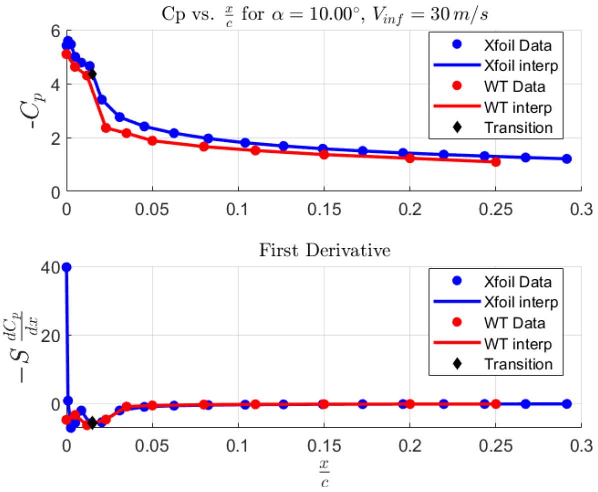

Figure 10: $C_p$ and $dC_p/dx$ of the upper surface for the first 30% of the chord, both XFOIL and WT experiments distribution at U = 30 $m/s$, $\alpha = 10°$. XFOIL transition point denoted by black diamond.

From Fig. 10, we can see that XFOIL predicts the transition point at the point of the minimum of $-C_p'$ value. Similarly, the results are consistent for other velocities and angles of attack, as shown in Fig 11 for $U = 30\,m/s, \alpha = 8°$ and for $U = 40\,m/s, \alpha = 10°$. Therefore, we can confidently trust the pressure coefficient from XFOIL for the derivative calculations of pressure profile. Therefore, in the results to come in the following subsection, we will focus mainly on the XFOIL pressure distribution data as we can control the grid size while constantly verifying the result against our WT experiments data.

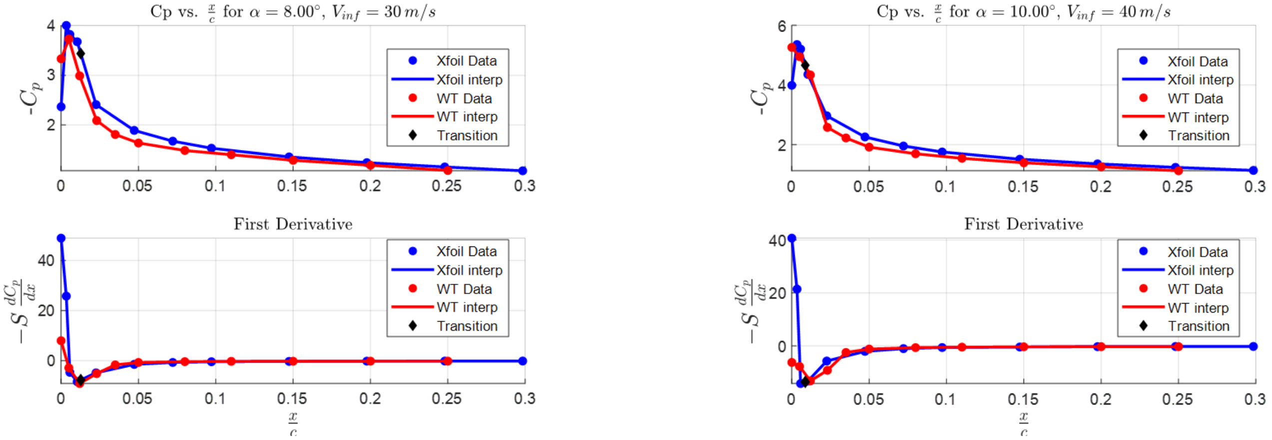

(a) $U = 30\,m/s, \alpha = 8°$.

(b) $U = 40\,m/s, \alpha = 10°$.

Figure 11: $C_p$ and $dC_p/dx$ of the upper surface for the first 30% of the chord, both XFOIL and WT experiments, XFOIL transition point denoted by black diamond.

### 4.1.3 Separation bubble identification from pressure profile data

Herein, we focus our analysis on identifying the laminar separation bubble (LSB) from the pressure profile and its derivatives following the approach used in (Simmons et al. 2024). We analyze first the pressure profile near the leading edge part of the wing. We note that these observations are mainly deduced from XFOIL data, as the WT experimental data were too sparse for such an analysis.

In Fig. 12a, we consider the case of $\alpha = 10°, U = 30$ m/s, where we can observe the effect of a suspected separation bubble in the approximate range of $0.01 < x/c < 0.2$. We can detect the separation region corresponding to the plateau in the pressure profile (as illustrated in Fig. 2 of (Russell 1979) study). Right after the peak of $-C_p$ profile, we have the separation point (denoted by $S$). Following that we have the transition point, also detected by XFOIL (and denoted via black diamond symbol), and lastly the reattachment point (denoted by $R$). The pressure derivatives in Fig. 12b are also used to locate the separation and reattachment point at the peaks in the second derivative. In particular, one can see that the plateau region is confined between two maxima picks of $-C_p''$ profile and between the maximum and minimum points of $-C_p'$ profile, in agreement with Simmons et al. (2024).

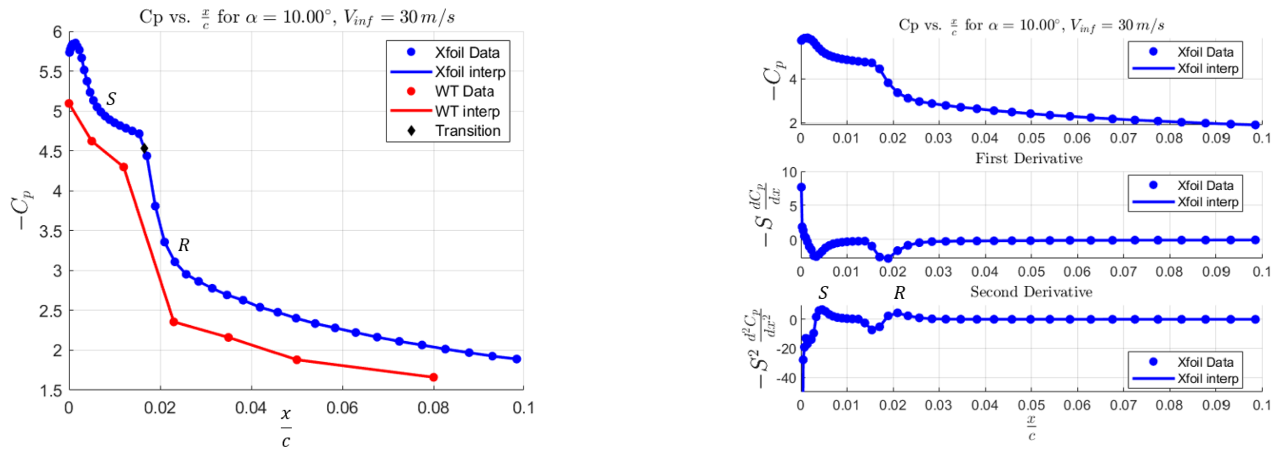

(a) $\alpha = 10°, U = 30$ m/s.

(b) $\alpha = 10°, U = 30$ m/s.

Figure 12: Pressure distribution for the upper surface, focusing on the first 10% of the chord length at $U = 30$ m/s and $\alpha = 10°$.

In Fig. 13we show two additional cases at for $U = 30$ and 40 m/s, for $\alpha = 12°$, where similar results are observed. We note that for the $U = 30$ m/s case, the XFOIL analysis closely follows the WT experimental data trends, whereas in the $U = 40$ m/s case, the observed plateau in $C_p$ profile is not evident in experimental profile. This can be due to either a lack of data points to capture the plateau region via experimental measurements.

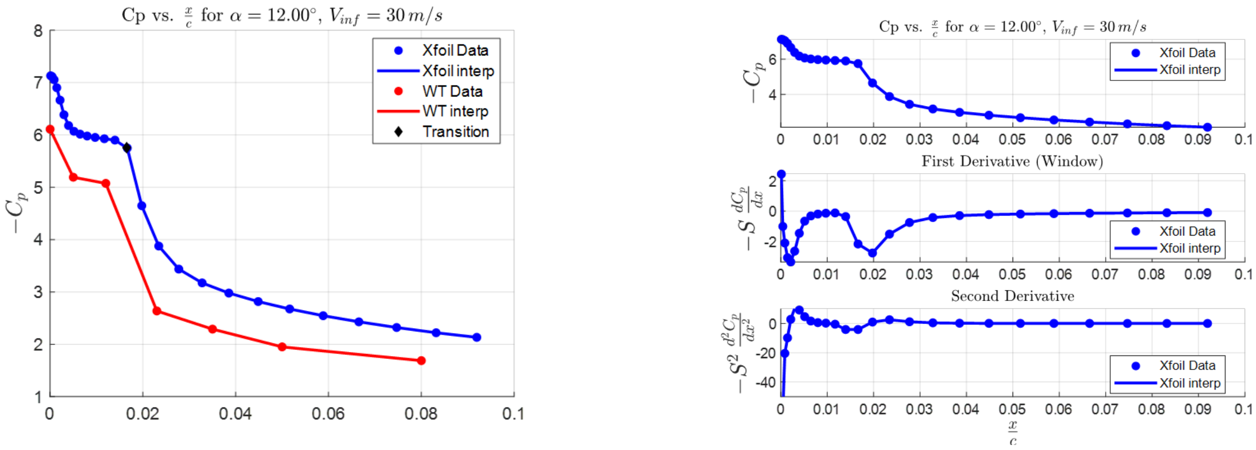

(a) $C_p$ vs. $x/c$ for the LE at $U = 30$ m/s and $\alpha = 12°$.

(b) $C_p$ derivatives vs. $x/c$ for the LE at $U = 30$ m/s and $\alpha = 12°$.

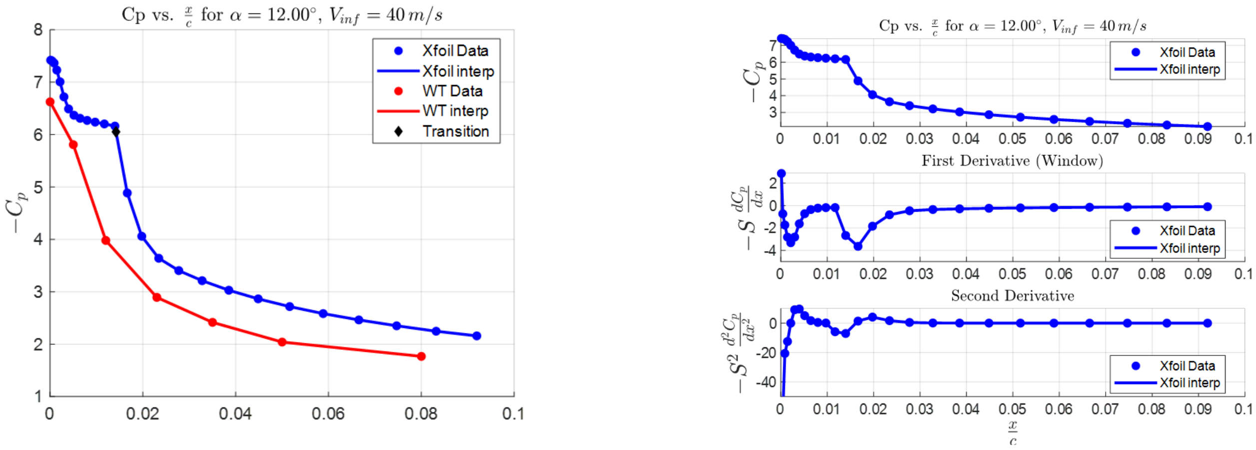

(c) $C_p$ vs. $x/c$ for the LE at $U = 40$ m/s and $\alpha = 12°$.

(d) $C_p$ derivatives vs. $x/c$ for the LE at $U = 40$ m/s and $\alpha = 12°$.

Figure 13: Pressure distribution for the upper surface, , focusing on the first 10% of the chord length.

Fig. 14 shows that for $\alpha = 14°$, the experiments do not agree with the XFOIL results. In particular, For angle of attack $\alpha = 14°$ and $U = 30$ m/s, in Fig. 14b, we can see a total plateau in the pressure coefficient in experiments, which indicates there is a completely stalled flow. In contrast, for angle of attack $\alpha = 14°$ and $U = 40$ m/s, we can see in Fig. 14a that the plateau is not captured in the WT experimental data. This difference between XFOIL and the WT experimental data may be due to inaccuracy in the transition detection for the XFOIL analysis. XFOIL predicts a laminar boundary layer at the LE, then a LSB leading to a turbulent boundary layer. In contrast, the WT experimental data show a turbulent boundary layer possibly immediately from the leading edge without triggering flow separation.

### 4.1.4 Separation detection after transition to turbulence

After observing a laminar separation bubble at the leading edge region, the flow transitioned to turbulent flow, and a second separation was observed at certain angles of attack. In particular,

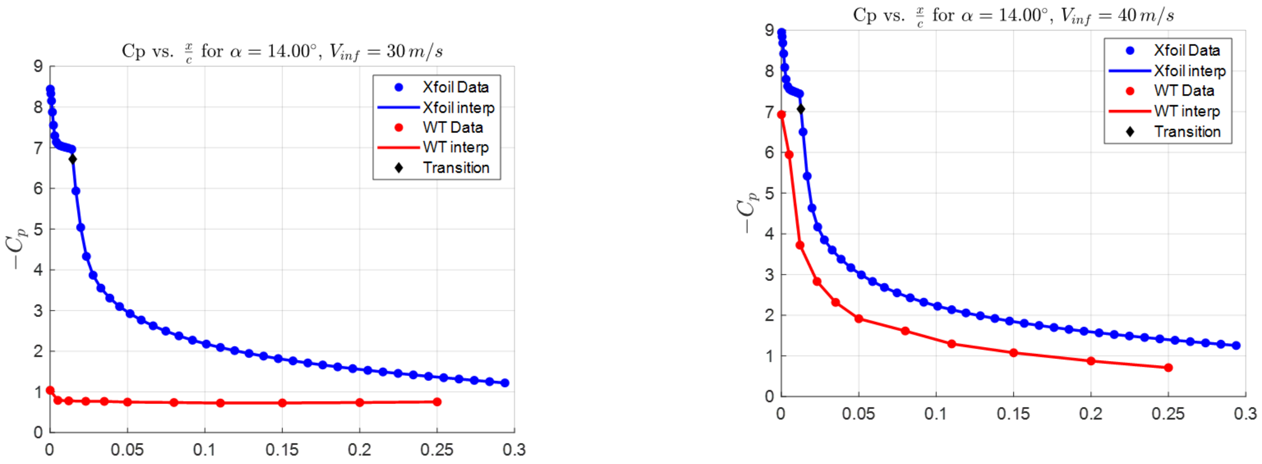

(a) Separation bubble $\alpha = 14°, U = 30$ m/s.

(b) Separation bubble derivatives $\alpha = 14°, U = 40$ m/s.

Figure 14: Pressure distribution for the upper surface, first 30% of the chord. Used for separation bubble identification.

Similarly to locating the separation bubble from the pressure derivatives, we can detect the separation of the turbulent boundary layer from the local minimum of the second derivative, as proposed in Simmons et al. (2024). Observing the pressure derivatives at the middle part of the airfoil (x/c=0.3-0.8) in Fig. 15, we can identify the suspected separation further downstream at x/c= 0.44 corresponding to min of $-C_p''$, which in agreement with the result of Simmons et al. (2024), where the authors associated the separation point of turbulent flow to second derivative of pressure profile. Similar results are also obtained for $\alpha = 12°, U = 30$ m/s and $\alpha = 12°, U = 40$ m/s, as shown in Fig. 21. This location of turbulent separation was also verified via oil flow visualizations that are discussed in the following section. Similar trends observed for additional case in Appendix 7.1.

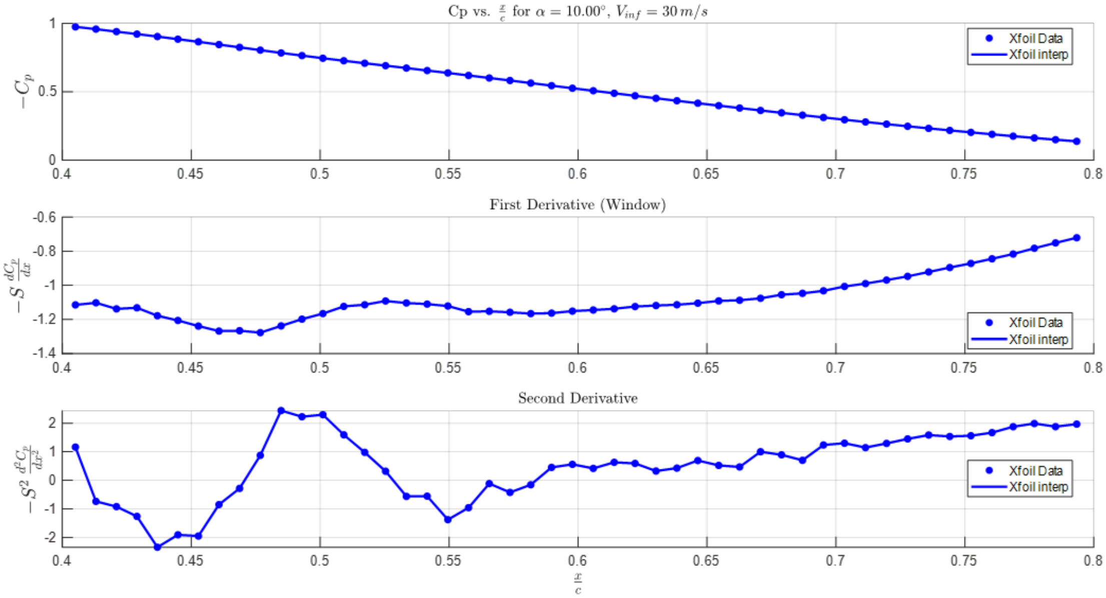

Figure 15: Pressure derivatives at separation point for $U = 30\,m/s, \alpha = 10°$.

## 4.2 Oil visualization

In this section, results from oil visualizations are presented. First, we identify the laminar separation bubble by looking at the case where $U = 30$ m/s and $\alpha = 10°$, we obtained a few images that capture both the separation bubble and the separation point further downstream. Looking at Fig. 16, we notice two different types of streamlines visible. The first and most obvious are the white streaks, which indicate that the oil droplet is carried by the flow and attached to the surface. The second and more indicative streamlines are the transparent lines visible at the top part, near the LE. These streamlines are created as the oil evaporates from the surface in the first five minutes of the experiment. We can see that the streamlines going from left to right stop around the $40\% - 50\%$ mark (each yellow line represents 10% of the chord). This separation line corresponds to pressure derivatives in Fig. 15, where $C_p''$ is at its local minimum at $x/c = 0.44$. After 50% of the chord, we can observe no coherent streamlines, indicating a detached flow region. Zooming for experiment at $U = 30$ m/s and $\alpha = 10°$ in Fig. 17, we can see that the streamlines are visible at the start, then as the flow separates the white streaks stop, and a patch of oil droplets appears with no streaks. Afterwards, the flow is reattached to the surface and the streamlines resume. Similar trends observed for additional case in Appendix 7.1.

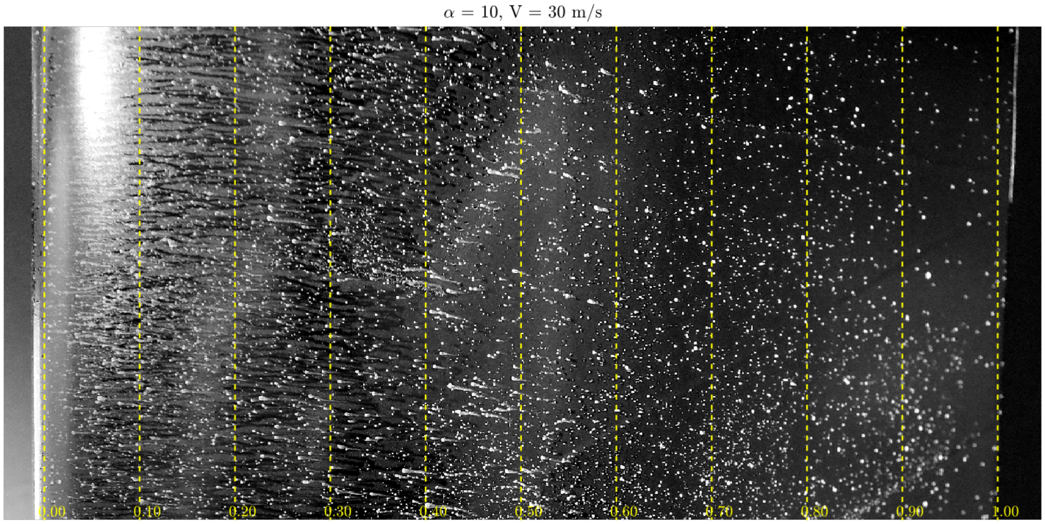

Figure 16: Oil visualization $U = 30$ m/s, $\alpha = 10°$, each yellow dashed line represents 10% of the chord from the LE at the left to the TE at the right.

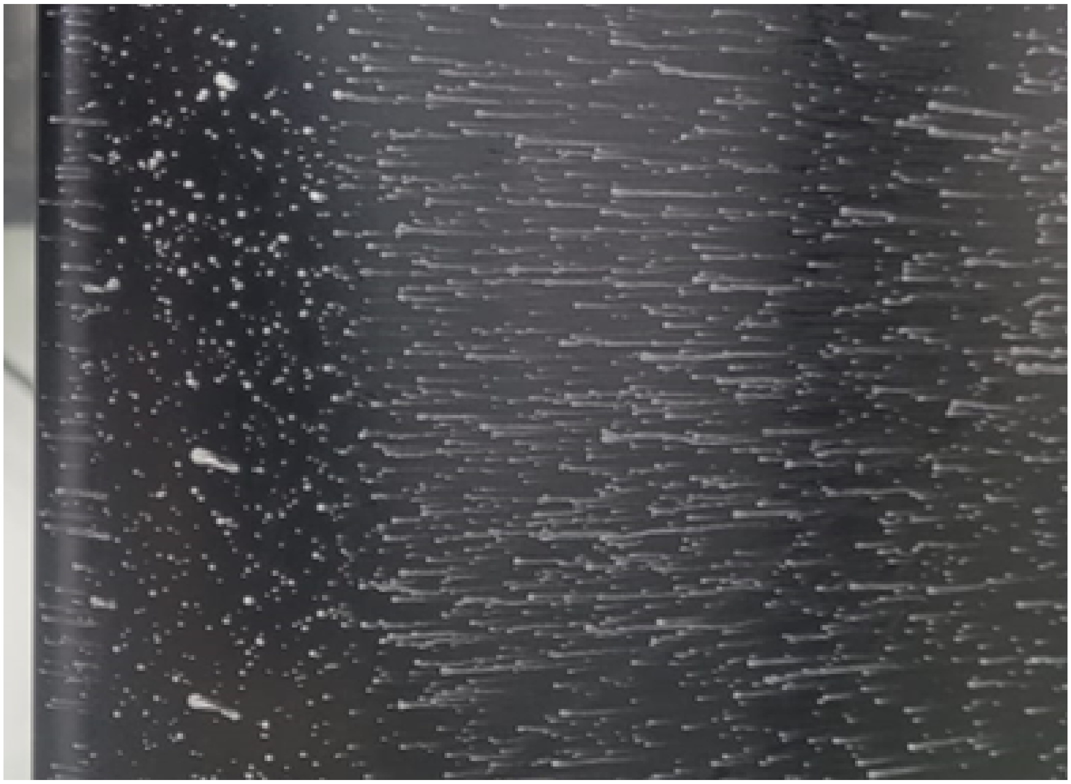

Figure 17: Zoom in of separation bubble $U = 30$ m/s, $\alpha = 10°$.

## 4.3 Drag calculation from wake measurements

In our study, we also evaluated the drag of the airfoil from wake pressure measurements. In Fig. 19, we can see an example of the measurements from the WT experiments of the total pressure distribution at the wake, including a single static pressure at the wake value as described in section 2.3.2. Using Eq. 1, we calculated the drag for each angle of attack. In Fig. 20a, we observe a 'parabolic' profile of the drag coefficient as a function of the angle of attack for $U = 30$ m/s. At $\alpha = 14°$, we can see the stalling of the airfoil as the drag coefficient increases by one order of magnitude.

Looking at the results for high freestream $U = 40$ m/s in Fig. 20b, we can see that there is no observed stall as there is no rapid increase in drag. At higher angles of attack, the maximum of the drag coefficient is observed at $\alpha = 10°$ and decreases for higher angles afterwards. Further studies, repeating these experiments are required to determine the reason for such behavior.

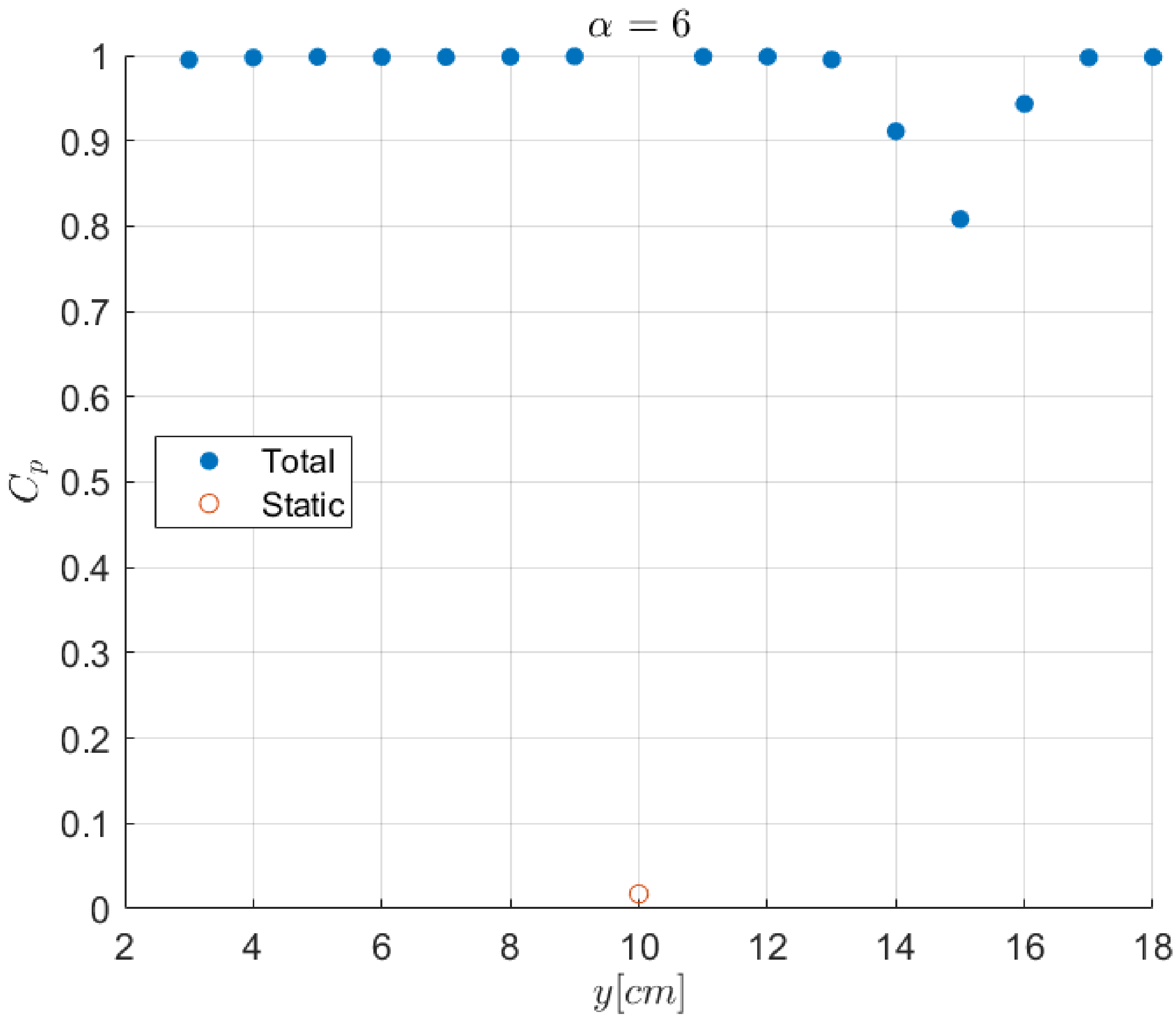

Figure 18: Wake example from WT experiments experiment at $\alpha = 6°$, 15 total pressure and one static pressure measurements.

Figure 19: Experimental examples of total pressure distribution at the wake of an airfoil.

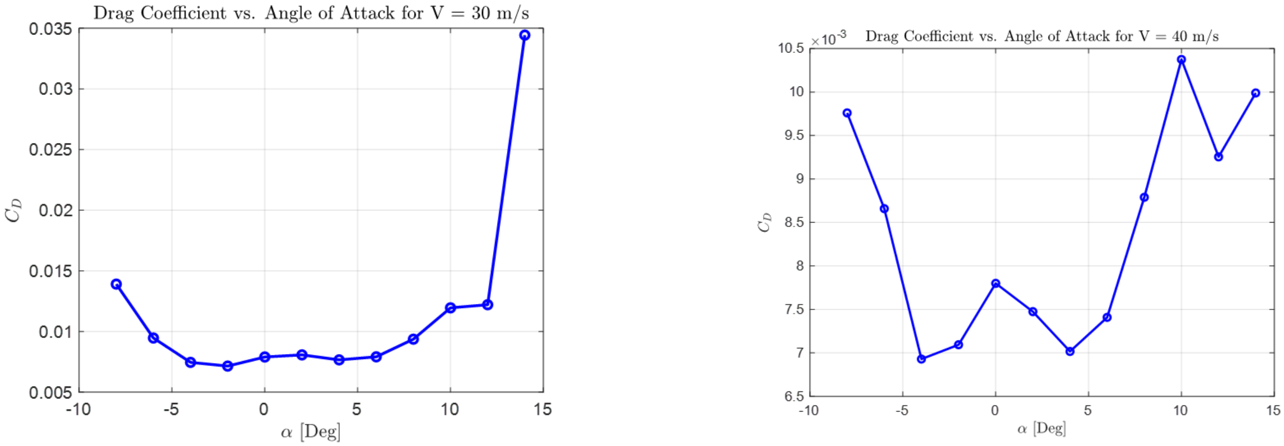

(a) $C_D$ vs. $\alpha$, $U = 30$ m/s.

(b) $C_D$ vs. $\alpha$, $U = 40$ m/s.

Figure 20: Drag coefficient $C_D$ vs. AoA $\alpha$ for different freestream velocities.

# 5 Conclusion

Laminar separation bubbles occur at low Reynolds numbers, such as UAVs and turbomachine blades. Identifying the laminar separation bubbles is essential to prevent their adverse effect on flow performance. In Simmons et al. (2024), it is shown that the first and second spatial derivatives of the streamwise static surface pressure profile are sufficient to determine key locations of detachment and reattachment in smooth body turbulent separation flow. In this project, we focused on exploring the streamwise variation of $C_p(x)$,$C_p'(x)$, and $C_p''(x)$ to detect the separation and reattachment locations of separation bubble in low Reynolds airfoil flow—a more complex case that may include a combination of laminar flow, laminar separation bubble, transition to turbulence and turbulent separation.

Experiments are performed over NACA 63-412 in subsonic open-return wind tunnel (tunnel No. 14), for freestream velocities in range of U = 10 - 40 m/s that corresponds to $Re = 1.7\times10^5 - 7\times10^5$, and for airfoil angles of attack (AoA) in range $\alpha = -14° - 14°$. We studied flow separation over a low Reynolds airfoil using surface pressure measurements, surface oil visualizations, and panel code analysis (XFOIL). The XFOIL data is used to achieve adequate spatial resolution for taking derivatives of $C_p$ after validating their agreement with experimental data.

We demonstrate that we can gain insights into the separation flow physics over the airfoil using surface pressure data, including the transition to turbulence, detachment, and reattachment locations of the separation bubble. In detail: first, a correlation between the peak of the first derivative and the transition point is observed for the considered velocities and angles of attack. Second, the separation bubble is determined to be between the two local maxima of the $-C_p''$ profile in agreement with the findings of Simmons et al. (2024) for a turbulent separation bubble.

Future extension of this study will focus on the application of Particle Image Velocimetry (PIV) for characterizing the unsteady physics of the separation bubble and associating the off-surface separation flow topology from PIV with on-surface flow topology obtained via oil flow visualizations and surface pressure measurements.

# References

Jewel B Barlow, William H Rae, and Alan Pope. *Low-speed wind tunnel testing.* John wiley & sons, 1999.

M Carreño Ruiz, L Renzulli, and D D'Ambrosio. Airfoil optimization for rotors operating in the ultra-low reynolds number regime. *Physics of Fluids*, 35(10), 2023.

Mark Drela. Integral boundary layer formulation for blunt trailing edges. In *7th Applied Aerodynamics Conference*, page 2166, 1989a.

Mark Drela. Xfoil: An analysis and design system for low reynolds number airfoils. In *Low Reynolds Number Aerodynamics: Proceedings of the Conference Notre Dame, Indiana, USA, 5–7 June 1989*, pages 1–12. Springer, 1989b.

Eltayeb M Eljack. The structure and dynamics of the laminar separation bubble. *Journal of Fluid Mechanics*, 998:A56, 2024.

Hui Hu and Zifeng Yang. An experimental study of the laminar flow separation on a low-reynolds-number airfoil. 2008.

I Karasu, MS Genç, HH Açikel, et al. Numerical study on low reynolds number flows over an aerofoil. *J. Appl. Mech. Eng*, 2(5):1000131, 2013.

Bjoern F Klose, GR Spedding, and Gustaaf B Jacobs. Flow separation, instability and transition to turbulence on a cambered airfoil at reynolds number 20 000. *Journal of Fluid Mechanics*, 1009:A9, 2025.

JCPJ Morgado, R Vizinho, MAR Silvestre, and JC Páscoa. Xfoil vs cfd performance predictions for high lift low reynolds number airfoils. *Aerospace Science and Technology*, 52:207–214, 2016.

Karthikeyan Natarajan, Sudhakar Senthamarai, and Paul Pandian Suriyanarayanan. Experimental studies on the effect of leading edge tubercles on laminar separation bubble. 02 2021.

John M Russell. Length and bursting of separation bubbles: a physical interpretation. *NASA. Langley Res. Center The Sci. and Technol. of Low Speed and Motorless Flight, Pt. 1*, 1979.

Hermann Schlichting and Klaus Gersten. *Boundary-layer theory.* springer, 1999.

DJ Simmons, FO Thomas, TC Corke, and I Gluzman. Experimental characterization and similarity scaling of smooth-body flow separation and reattachment on a two-dimensional ramp geometry. *Journal of Fluid Mechanics*, 1000:A12, 2024.

J Tank, Lelanie Smith, and GR Spedding. On the possibility (or lack thereof) of agreement between experiment and computation of flows over wings at moderate reynolds number. *Interface focus*, 7(1):20160076, 2017.

Connor E Toppings and Serhiy Yarusevych. Laminar separation bubble formation and bursting on a finite wing. *Journal of Fluid Mechanics*, 986:A26, 2024.

# 6 Acknowledgments

The authors wish to thank Mechanics Laboratory (FMlab) team, especially to Mark Kiselev—lab engineer of FMlab, for their assistance in designing and constructing the experimental set-up. Also, the help of the staff of the Wind Tunnel Complex of the Technion's Faculty of Aerospace Engineering is gratefully acknowledged.

# 7 Appendix

## 7.1 Separation line detection

Here we'll show additional cases in which the local minimum of $C_p''$ corresponds to the separation line, as seen in Fig. 21 and Fig. 22 for $\alpha = 12°$ and $U = 30, 40\, m/s$.

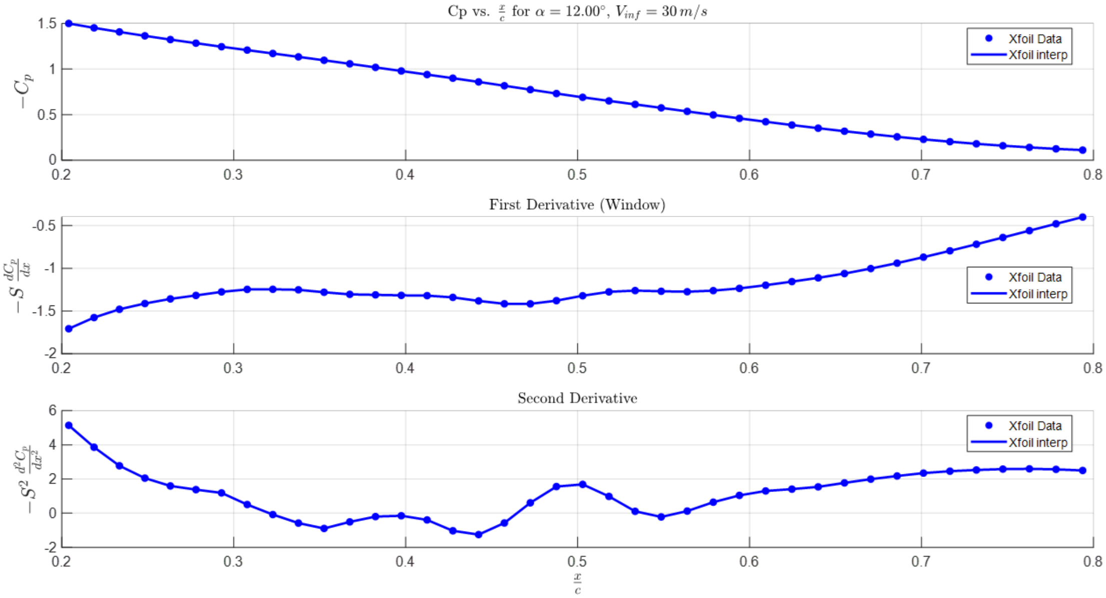

(a) Pressure derivatives at separation point for $U = 30\,m/s, \alpha = 12°$.

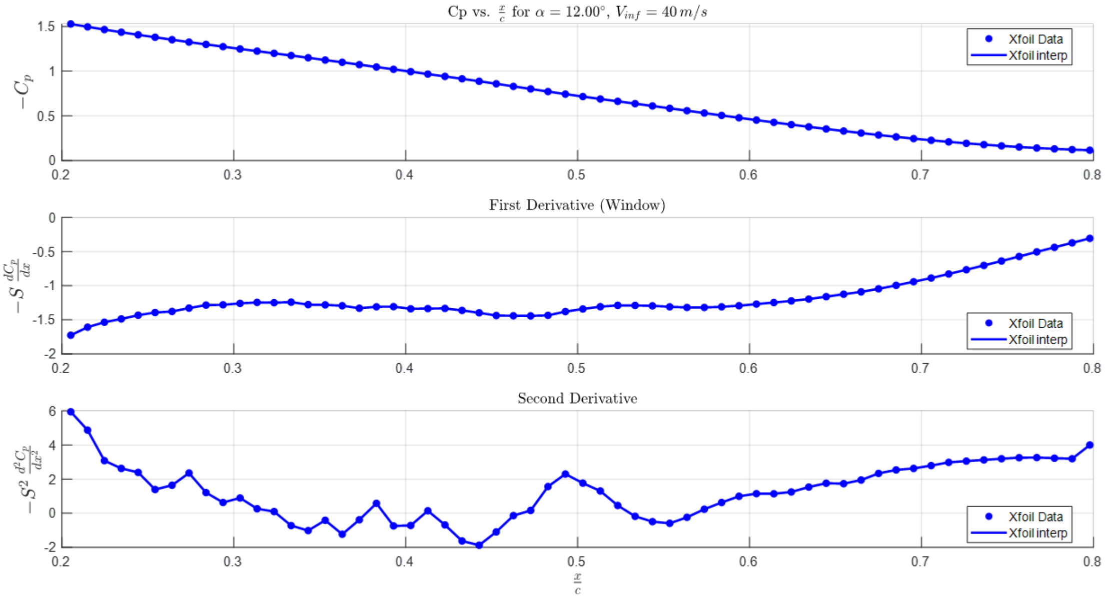

(b) Pressure derivatives at separation point for $U = 40\,m/s, \alpha = 12°$.

Figure 21: $C_p(x)$,$C_p'(x)$, and $C_p''(x)$ between 40% and 80% of the chord.

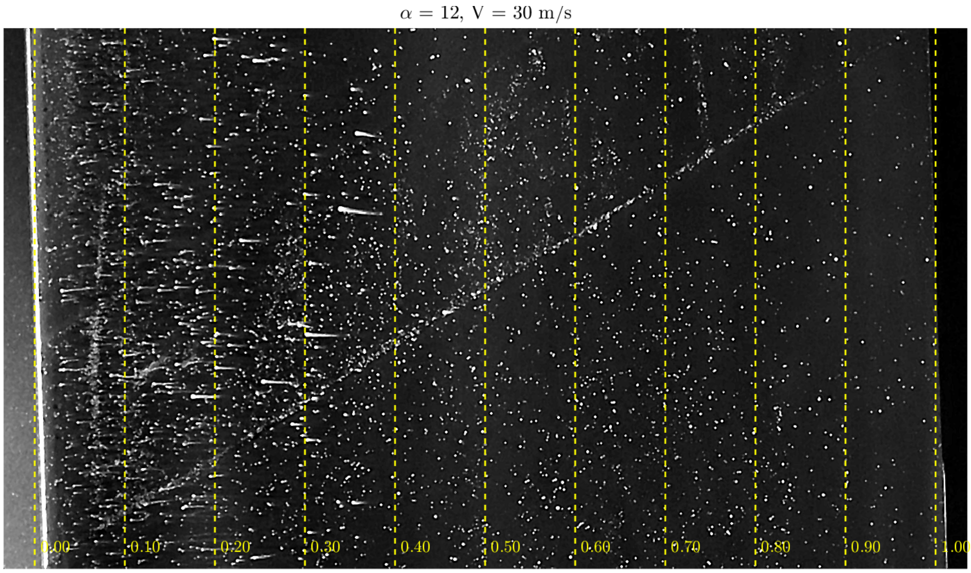

(a) Oil visualization $U = 30$ m/s, $\alpha = 12°$, each yellow dashed line represents 10% of the chord from the LE at the left to the TE at the right.

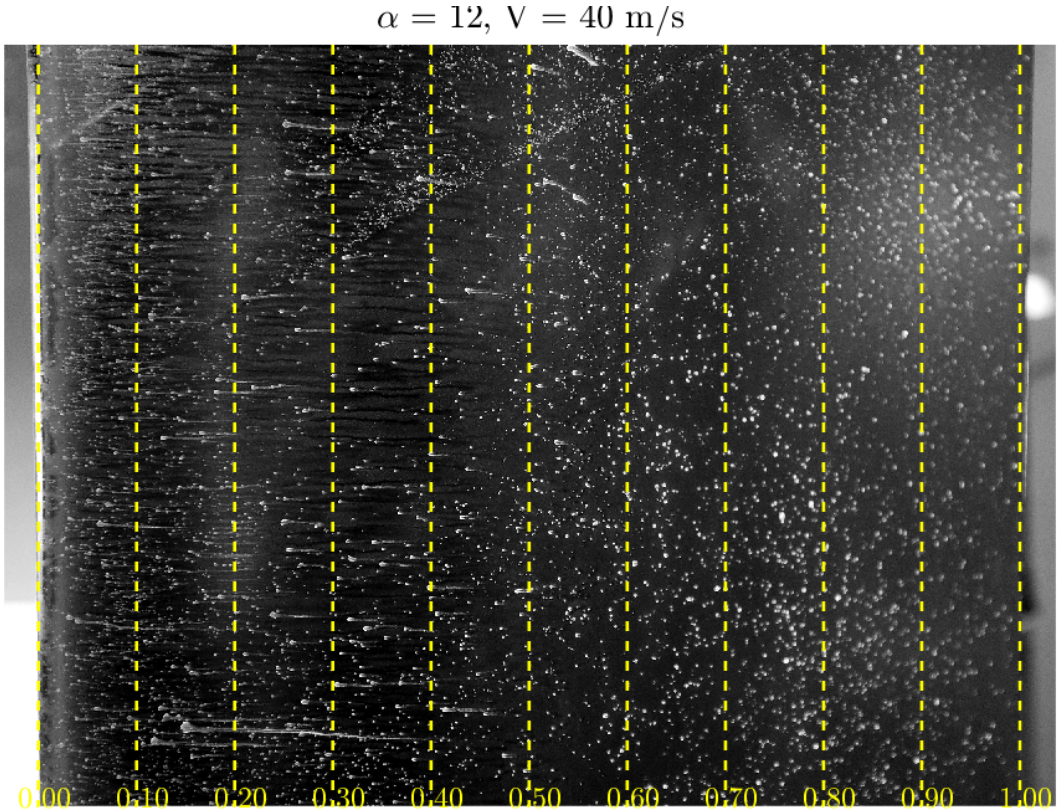

(b) Oil visualization $U = 40$ m/s, $\alpha = 12°$, each yellow dashed line represents 10% of the chord from the LE at the left to the TE at the right.

Figure 22: Oil visualization for additional cases.